

Preparation and characterization of Fe-incorporated TiO₂ thin films: A study of optical constants and dispersion energy parameters

Tapash Chandra Paul^{1,2}, Jiban Podder^{2*}, Lincoln Paik³

¹Department of Physics, Jagannath University, Dhaka-1100, Bangladesh

²Department of Physics, Bangladesh University of Engineering and Technology, Dhaka-1000, Bangladesh

³Department of Physics, Bangladesh University of Textiles, Dhaka-1208, Bangladesh

*E-mail: jpodder59@gmail.com, ORCID ID: 0000-0002-4171-4785.

Abstract

In this study, we have delineated the preparation and influence of Fe doping on microstructural and optical properties of the pristine and Fe-incorporated TiO₂ thin film with different Fe concentrations (0, 2, 4, 6, and 8 at.%). The samples are prepared by easier and cost-saving way of spray pyrolysis technique (SPT) using Ti(OCH₂CH₂CH₂CH₃)₄ as a precursor of mother material. The effect of Fe in the microstructure and phase formation of TiO₂ thin films is investigated by XRD analysis. XRD investigation depicts that the pristine product corresponds to anatase phase of TiO₂ and remains uncontaminated with addition of 2 at.% Fe impurity. It is also observed that Fe introduces a phase transition from anatase to rutile after adulterating more Fe contents (4, 6 and 8 at.%). In order to study optical characteristics, UV–vis spectroscopy has been employed which reveals that UV absorption for the Fe incorporated TiO₂ products are noticed to move to a longer wavelength (red shift) and Fe contents lessen bandgap energy from 3.81eV (0 at.% Fe) to 3.70 eV (8 at.% Fe) of the TiO₂ thin films. The impact of Fe on the optical constants such as refractive index, complex dielectric constants, tanδ, VELF and SELF, dispersion parameters of obtained titanium dioxide samples has been studied. The results display that Fe influences the structural and optical characteristics significantly.

Keywords: SPT; Williamson-Hall method; Dielectric constants; Dispersion constants; Optoelectronic applications.

1 Introduction

With the development of the applications such as LEDs [1], supercapacitor [2], gas sensor [1], anti-reflective coatings [3], optical waveguides [4], optoelectronics [5], photonic crystals [6] and semiconductor-based device structures [7], transition conducting oxide (TCO) thin films have recently grabbed the concentration of the scientists as a prospective contestant. Among the oxide materials, there is a considerable research focus on TiO_2 since it becomes one of the fascinating transition metal oxides which has enticing physical and chemical features due to its broad transmittance ($\sim 80\%$), a wideband gap, high refractive index, fairly good thermal and chemical stabilities [8][9]. The TiO_2 crystalline structure has three different phases including anatase, rutile, and brookite. TiO_2 having anatase phase as a TCO has numerous advantages due to its relative low effective mass, low cost and stability in a hydrogen plasma atmosphere which is used to produce solar cells [10]. There is an important evolution to refrain the microstructural and optical properties of TiO_2 in order to utilize a highest solar spectrum for the different applications to resolve our environmental problems [11]. Doping with more foreign elements (Zn, Mn, Fe, Ni, Co) of TiO_2 nanoparticles affects their optical and structural properties which allows to adapting them for a variety of applications [12]. Kim et al. [13] investigated the formation of TiO_2 doping with Fe content by mechanical alloying and represented the photocatalytic characteristics and microstructural analysis. They noticed that Fe shows a remarkable impact on the bandgap energies which varies 2.5–2.9 eV. Patil et al. [14] used spray pyrolysis route to synthesize the Ni-doped titanium dioxide and reported that Ni doping changed the surface morphology of the deposited products. Hough et al. [10] employed RF magnetron sputtering for the synthesis of TiO_2 samples and they revealed that the incorporation of Mo enhances the crystallization and increases the grain size. We have taken Fe as a dopant element because the size of Fe^{3+} (0.64 Å) [15] and Ti^{4+} (0.68 Å) [16] is almost similar and it has a static half-filled d^5 electronic configuration [17]. However the presence of Fe as an intrinsic impurity and extrinsic dopant has influence on structural, optical and electrical properties [18].

In view of doping applications, number of techniques have been reported in the literature for the fabrication of Fe-doped TiO_2 thin films which includes pulsed laser deposition method [19], spin coating technique [20], magnetron sputtering [21], electrochemical deposition [22], hydrothermal method [23], sol-gel [24], chemical bath deposition (CBD) [25] etc. In this article we have employed the SPT for numerous advantages. This method is simple and cost effective to synthesize in small dimensions and at a large areas and produced samples are almost uniform and reproducible [26].

The current research focuses on the formation of titanium dioxide thin films as a function of Fe and impact of Fe contents on microstructural and optical characteristics. We have employed W-H and H-W techniques along with Scherrer formula to find the numerous microstructural parameters taking into consideration line broadening. To best of our concern, no systematic reports on the measurement of optical parameters and dispersion energy parameters as function of Fe impurities have been published. Thus the present researchers have given a deep attention on the on the subject of E_g , refractive index, dielectric constants,

dielectric loss, average values of oscillator strength, VELF and SELF of the samples. The observations reflect that the as-prepared products might have a good potential as an emerging aspirant for optoelectronic applications.

2 Experimental details

2.1 Materials

The preliminary solution for the preparation of pristine TiO₂ thin film consisted of Titanium butoxide of 0.1M concentrations. The spray pyrolysis system used the ferric chloride as the raw chemical of dopant with the starting solution to obtain the Fe doped products. A little bit of hydrochloric acid (nearly 1.2 mL) was dissolved with both solutions to get consistent solutions. The purity of the materials is 97%, 98%, and 37% respectively. Deionized water was used in all cases of the current research.

2.2 Synthesis of TiO₂ thin films:

The deposition of pristine and Fe doped samples has been carried out in a simple and low-cost fume chamber as illustrated in **Figure 1** [27] and the detail of the deposition technique is presented in **Table 1**.

Table 1. Detail of the TiO₂ deposition process.

Deposition parameters	Optimum value
Substrate	microscope slides
Base pressure	0.5 bar
Deposition time	10±2 min.
Deposition rate	0.5 mL/min
Nozzle to substrate separation	30 cm
Amount of solution	100 mL
Doping (Fe) concentration (at. %)	2.0, 4.0, 6.0, 8.0
pH	5.5

In this method, first, a solution of initial precursor material titanium butoxide with appropriate concentration (0.1 M) is obtained into 100 mL de-ionized water in a beaker at room temperature. The initial mixture has been stirred for about one to two hours employing a magnetic stirrer to achieve a harmonized solution. In addition, 1.2 ml amount of HCl was mixed with preceding solution that makes it aqueous. In parallel way, the desired amounts of doping material ferric chloride based on the Fe concentration varied in the range 0–8 at% with an interval 2 is adopted to the resulting solution prior to stirring the solution thoroughly to have the doped products. The glass slides used as substrates during the deposition process are introduced after cleaning employing acetone and de-ionized water successively to eradicate pollutant. The substrate temperature remains 450 °C in the time of spraying controlled with the help of a Copper- Constantan thermocouple. The synthesis process has been displayed in Figure 2 schematically.

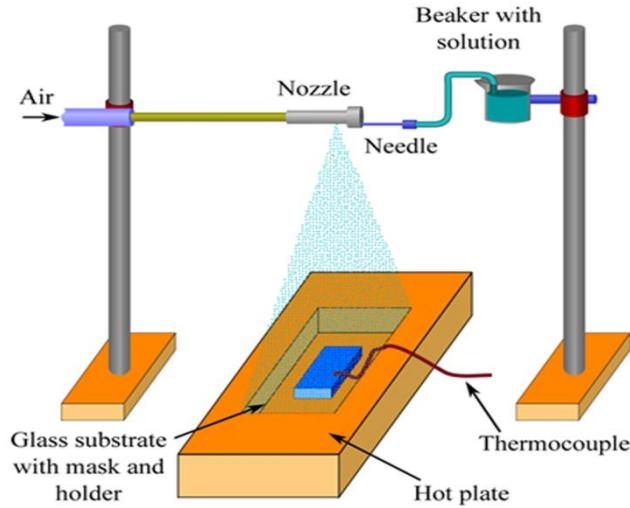


Figure 1. Experimental setup of the spray pyrolysis technique.

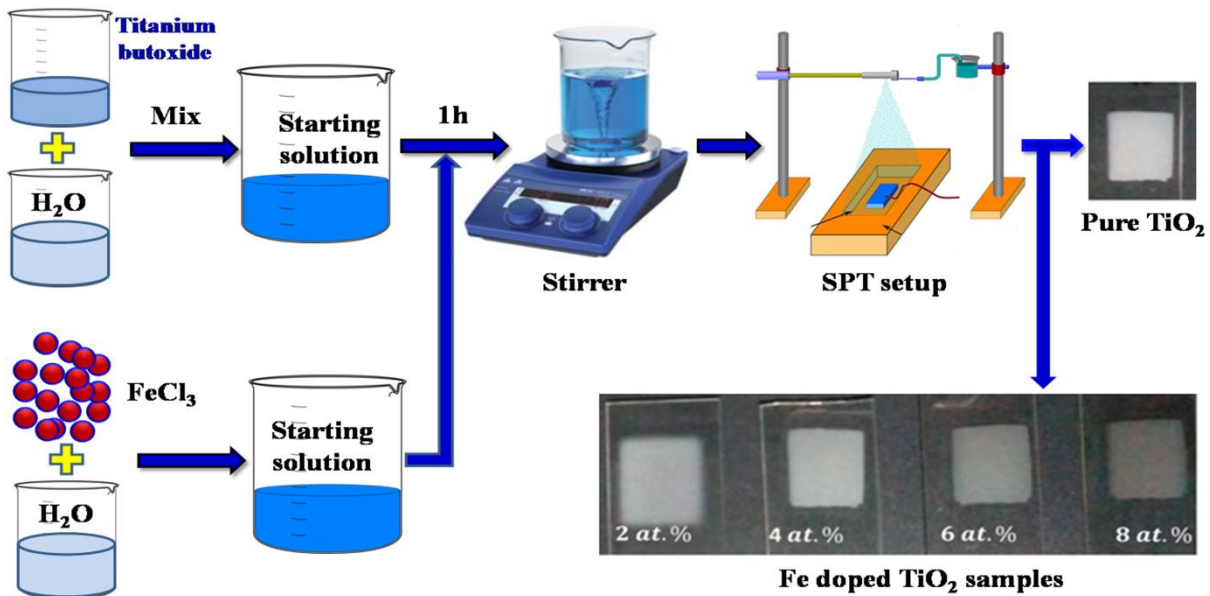
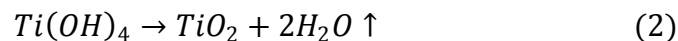


Figure 2. A plausible diagram of pristine and Fe-doped TiO₂ thin films

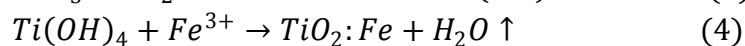
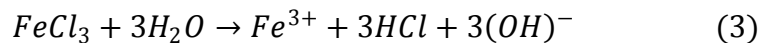
The formation of metal oxide (TiO₂) particles has been occurred by hydrolysis of metal alkoxides. The following overall reaction between Ti (IV)-butoxide (precursor) and water (reactant) that could occur on hot substrate resulting in the formation of TiO₂ thin film are given as follows.



TiO₂ is, then, formed by the condensation of the hydrolyzed species.



The possible chemical reactions during the formation of Fe doped TiO₂ thin films are given below.



Hence, the formation of corresponding oxide associated with Fe might not occur in the present research.

2.3 Characterization techniques

The resultant pristine and Fe doped thin films are undergone for their structural and optical characterizations. XRD diffractometer (3040XPertPRO, Philips) has been used to examine the crystallinity and phase identification. The absorbance spectra of the products are measured using a UV–Visible–NIR spectrophotometer.

3 Results and discussion

3.1 Microstructural investigations

Figure 3 displays the XRD patterns of all thin film samples of TiO₂, doped with Fe content of 0.0, 2.0, 4.0, 6.0 and 8.0 at.%. The obtained XRD peaks in **Fig. 3a** confirm the anatase phase of tetragonal crystal arrangement in pristine sample having space group I41/amd(JCPDS 21-1272) [28] and highly intensified peak indicates the good crystallinity of TiO₂ nanoparticles. The addition of 2 at.% Fe does not alter the lattice structure and phase. After that, with the introduction of further impurity level (Fe content i.e., 4, 6 and 8 at.% Fe) the pristine product is noticed to exhibit the mixed phase of TiO₂ and transform from anatase to rutile phase (**Figure 3a**).

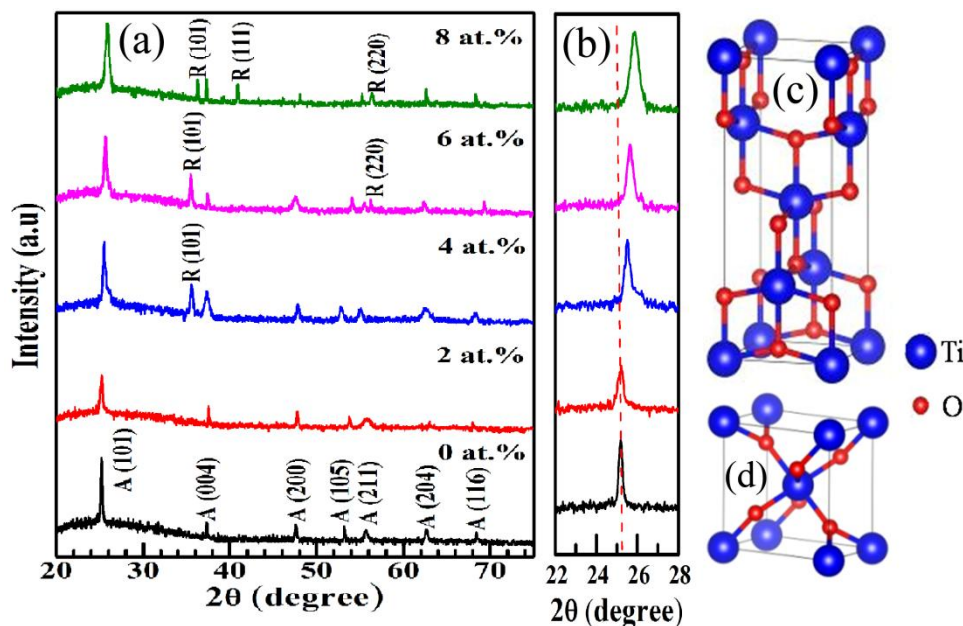


Figure 3. (a) XRD patterns of pristine and Fe doped TiO₂ thin films. (b) Magnification view of (101) plane (c) anatase and (d) rutile phases of TiO₂

The TiO₂ nanoparticles has constructive growth along (1 0 1) plane appearing preferential orientation along (1 0 1). The dominating peak is observed to shift toward higher 2θ positions as depicted in Fig. 3b confirming the conversion of anatase to rutile phase due to Fe content [29]. The anatase and rutile crystal structure of TiO₂ has been depicted in Fig. 3c and 3d, respectively.

3.1.1 Calculation of D using Scherrer formula:

To study the nanocrystalline properties of the material it is very crucial to study the crystallite size (D) and lattice strain (ϵ). Numerous techniques have been developed to estimate these characteristics. For the estimation of D values of bare as well as Fe-doped TiO₂, firstly we used FWHM, and the peak of the planes from the XRD data in the Debye-Scherrer equation [30],

$$D_S = \frac{K\lambda}{\beta_D \cos \theta} \quad (5)$$

Where D_S = crystallite size, λ = wavelength of x-ray radiation ($\lambda=1.54056 \text{ \AA}$ for Cu-K α), β_D = half-width full maximum, θ = Bragg's angle in degree and $K=0.09$. The estimated values of D_S are shown in Table 2. The variation of the crystallite size D and dislocation density has shown in Fig 4. It maintains the inverse relation. As the Fe contents increase in TiO₂ lattice the crystallite size decreases and dislocation density displays the opposite fashion.

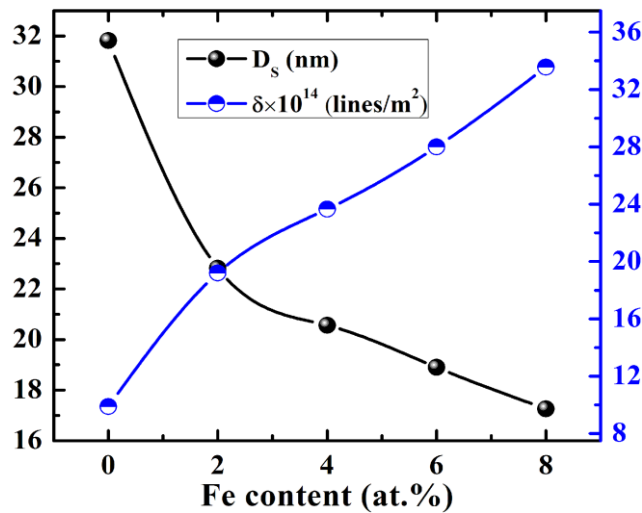


Figure 4. Variation of D obtained from Scherrer method and dislocation density as a function of Fe content

3.1.2 Measurement of D and ϵ using W-H technique

We have applied W-H technique to evaluate the value of the crystallite size and strain is the Williamson and Hall (W-H) method written as [31]

$$\beta \cos \theta = \frac{K\lambda}{D_{WH}} + 4\epsilon_{WH} \sin \theta \quad (6)$$

Where ϵ_{WH} is the strain and D_{WH} is the crystallite size. The above relation (6) is a linear equation like $y=mx+c$. We have taken $\beta_{hkl} \cos \theta$ in the y-axis and $4 \sin \theta$ is taken in the x-axis to fit the W-H plot. We have evaluated strain from the slope and crystallite size from the y-intercept. The relationship of D_{WH} , ϵ_{WH} and δ with Fe as doping element has been depicted in Fig 5.

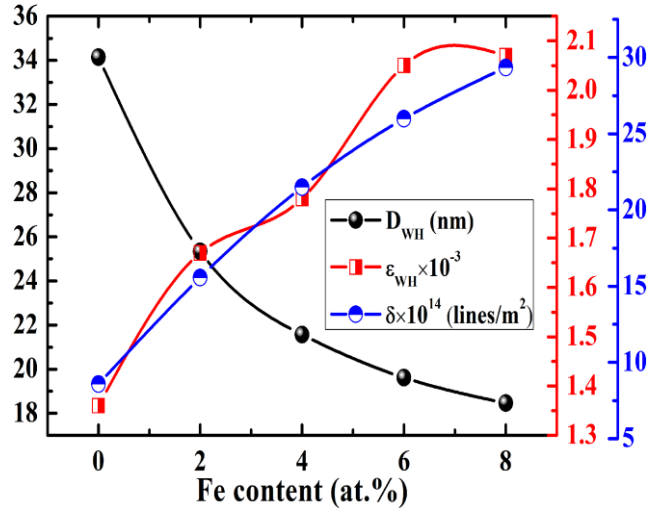


Figure 5. Variation of crystallite size, strain and dislocation density obtained from W-H plot.

3.1.3 Measurement of D and ϵ using H-W technique

The third method we have adopted for the estimation of D and ϵ is the Halder-Wagner (H-W) method that is expressed as [15].

$$\left(\frac{\beta}{\tan\theta}\right)^2 = \frac{K\lambda}{D_{HW}} \cdot \frac{\beta}{\tan\theta \sin\theta} + 16\epsilon_{HW}^2 \quad (7)$$

Where D_{HW} and ϵ_{HW} define the size and strain, respectively. The above equation is a linear plot of $\left(\frac{\beta}{\tan\theta}\right)^2$ vs $\frac{\beta}{\tan\theta \sin\theta}$ that is known as the H-W plot. We have determined D_{HW} from the slope of the straight-line plot and ϵ_{HW} from the y-intercept of the plot. The variation of D_{HW} , ϵ_{HW} and δ with Fe contents as a dopant has been delineated in Fig.6.

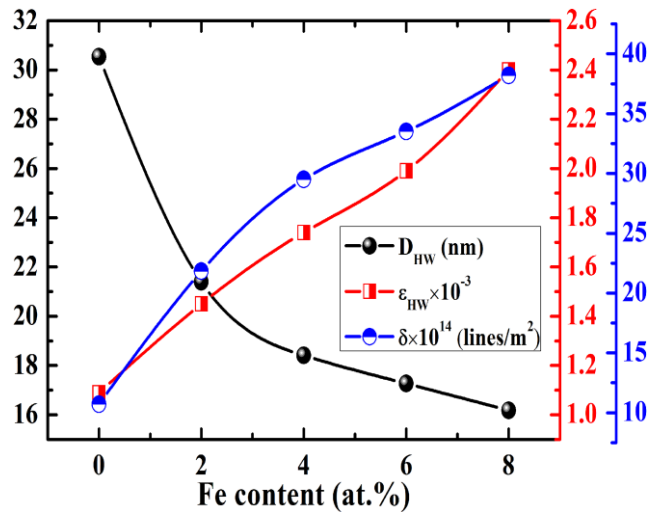


Figure 6. Variation of crystallite size, strain and dislocation density obtained from H-W plot.

3.1.4 Numerous microstructural parameters

The strain (ε) can be defined from the Stokes–Wilson formula[32]

$$\varepsilon = \frac{\beta_D}{4 \tan \theta} \quad (8)$$

in the above equation β_D =half with full maximum, and θ = Bragg's angle.

The dislocation density (δ) was determined by using the following equation[33]

$$\delta = \frac{1}{D^2} \quad (9)$$

here D = crystallite size.

Microstress(σ_s) has been computed using the following relation [34]

$$\sigma_s = \frac{\varepsilon}{2} E \quad (10)$$

In this equation ε = strain and $E=282.76$ GPa, Young modulus of the titanium oxide.

The interplanar spacing (d) can be estimated from Bragg's relation.

$$2d \sin \theta = n \lambda \quad (11)$$

The lattice parameter a=b and c can be estimated by the formula,

$$\frac{1}{d^2} = \frac{h^2 + k^2}{a^2} + \frac{l^2}{c^2} \quad (12)$$

(h, k, l)= Miller indices for Bragg's plane.

Table 2. Deviation of crystallite size and strain of the resulted TiO₂ products determined applying different methods.

Fe contents (at.%)	Microstress (GPa)	Strain $\varepsilon \times 10^{-3}$	Scherrer	W-H technique		H-W technique	
			formula D _S (nm)	D _{WH} (nm)	ε_{WH} $\times 10^{-3}$	D _{HW} (nm)	ε_{HW} $\times 10^{-3}$
0	-0.7041	4.98	31.82	34.14	1.36	30.54	1.09
2	-0.7903	5.59	22.82	25.34	1.67	21.40	1.45
4	-0.8214	5.81	20.56	21.57	1.78	18.41	1.74
6	-0.8865	6.27	18.90	19.62	2.05	17.27	1.99
8	-1.6895	11.95	17.26	18.46	2.07	16.18	2.40

The texture coefficient (TC) is estimated employing the equation below [35]

$$TC_{(hkl)} = \frac{I_{(hkl)}/I_{0(hkl)}}{\frac{1}{n} \sum I_{(hkl)}/I_{0(hkl)}} \quad (13)$$

Where $I_{(hkl)}$ = relative intensity and $I_{0(hkl)}$ = standard intensity of the (hkl) plane.

The values of stacking fault (SF) can be calculated using the following relation

$$SF = \left[\frac{2\pi^2}{45(3\tan\theta)^{1/2}} \right] \beta \quad (14)$$

The estimated values of the structural parameters are shown in Table 2 and Table 3

Table 3. Deviation of numerous structural parameters of bare and Fe-incorporated products

Fe contents (at.%)	δ (lines/m ²) $\times 10^{14}$			Lattice constants (Å)		Texture Coefficients	Stacking Fault
	Scherrer formula	W-H technique	H-W technique	a = b	c		
0	9.88	8.58	10.72	3.81	9.43	1.0829	0.002392
2	19.20	15.57	21.83	3.79	9.67	1.3334	0.003334
4	23.66	21.49	29.50	3.75	9.51	1.4318	0.003680
6	28.00	25.98	33.52	3.74	9.36	1.5187	0.003995
8	33.57	29.35	38.20	3.69	9.59	1.4548	0.004357

3.2 Dispersion of optical constants

Figure 7 presents the UV–vis absorption spectra of TiO₂ and Fe doped TiO₂ samples as a function of λ in the range of 300-1200 nm and exhibits the sharp absorption edges in the UV light region at around 450nm. The magnified result of absorbance upto 0.3 is depicted in the **Fig. 7**. The deposited TiO₂ products show an average absorption (0.12) between 500 nm and 1200 nm. The absorbance of 2 at.% Fe doped TiO₂ illustrates an enhancement characteristic and declines for the higher doping levels (4, 6 and 8 at.%). This reduction of absorbance values of doped products might be attributed to the increase of photon scattering by lattice defects induced from Fe impurity and result of the despair and passing of electrons from the VB to CB of TiO₂ crystal [36]. The Fe doping induces a red shift in the absorption edges i.e., the absorption edge is shifted towards the lower photon energy, which indicates the decrement in band gap. The shift of absorption edges appears in the iron doped TiO₂ products may be owing to the transfer of electrons from valence band to the conduction band of TiO₂ [37].

In order to evaluate the bandgap (E_g) values using the absorbance data, the plots of $(\alpha h\nu)^2$ as a function of $h\nu$ have been drawn in **Fig. 8** and expressed by Tauc's relationship [23]:

$$\alpha h\nu = A(h\nu - E_g)^{1/2} \quad (15)$$

where α is the absorption coefficient, A implies a constant, n implies an exponent, $n = 1/2$ for direct transition and $n = 2$ for indirect transition.

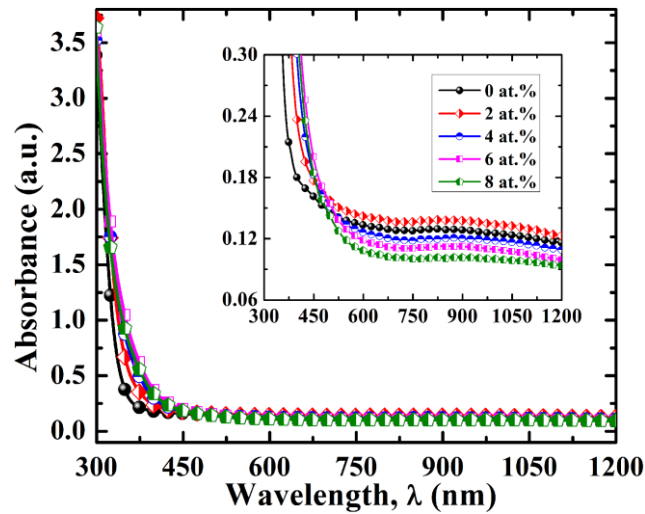


Figure 7. Wavelength dependent absorption behavior of pristine and Fe-incorporated titanium dioxide samples

We have given an attention to find the direct bandgap because of the values of n remains fixed inside the intended energy range [38]. The thin film's bandgap values have been determined as a result of extrapolating the linear part of the plot toward lower energies. The intercepts on $h\nu$ axis provides the E_g values which has varied from 3.70 eV to 3.81 eV. The obtained results of E_g in the current study are comparable to the range of E_g of TiO_2 reported in the literature [39]. The E_g values are influenced by the crystallinity of products. When the crystallite size decreases, the density of the grain boundaries increases and, as a result, more carriers are trapped in the space charge region, leading to a decrease in the free carriers. In addition, this decrement in E_g may be associated to the trapping level formed between the VB and CB of TiO_2 by Fe impurity (Fig. 9) [1][37].

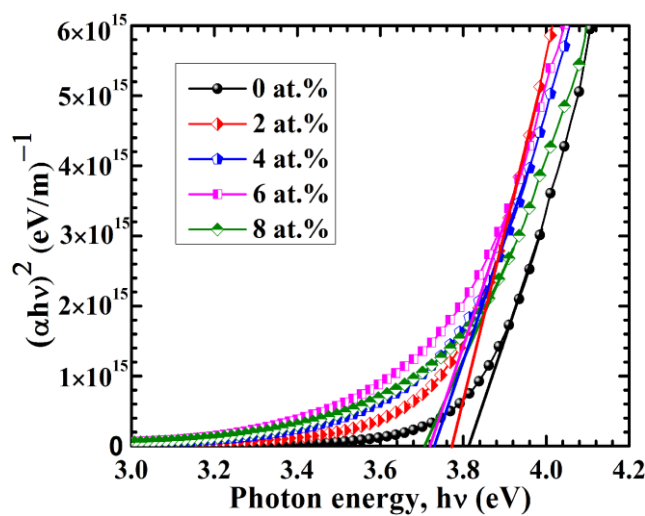


Figure 8. E_g of pristine and Fe doped TiO_2 thin films.

Refractive index (n) of the resultant pristine and Fe-doped products is obtained using the following relation [40].

$$n = \left(\frac{1+R}{1-R} \right) + \sqrt{\left(\frac{4R}{(1-R)^2} - k^2 \right)} \quad (16)$$

In this above equation (16), R is the reflectance of the TiO₂ thin film which is calculated from the T and A data.

The extinction coefficient (k) is also known as the attenuation coefficient, the loss of light energy per unit penetration in the medium, which also describes that amount of the light energy is absorbed when light travels through that medium. For the absorbing medium, the value of k is much higher than the transparent medium [36].

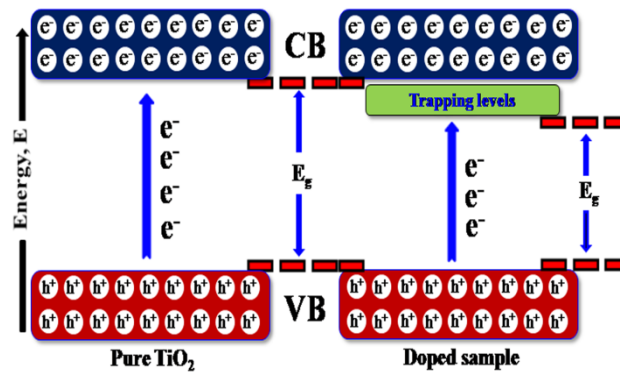


Figure 9. A hypothetical analysis of band gap structures of pure and Fe doped TiO₂

The extinction coefficient (k) of the prepared pure and doped samples can be measured using the following equation [41].

$$k = \frac{\alpha\lambda}{4\pi} \quad (17)$$

where α is the absorption coefficient, and λ is the wavelength of the radiation.

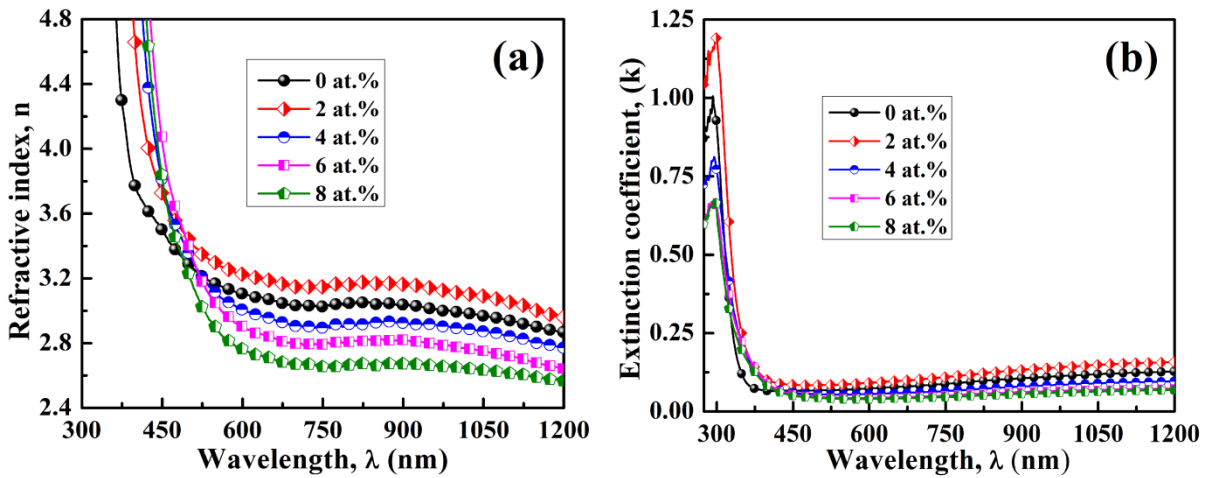


Figure 10. (a) Deviation of n and (b) k with λ for Fe doped TiO₂ thin films with various Fe concentrations

The variation of refractive index (n) and extinction coefficient (k) with wavelength λ is given in Figure 10. In the case of 2% Fe-doped TiO_2 film the value of n and k increases. This can be explained as the decrease of the grain size when Fe is incorporated [42]. After that with the increase of Fe content in the sample (4, 6, 8 at.% Fe-doped TiO_2), n and k are noticed to decline. This decrease of n and k can be subjected to the increase of carrier concentration in the highly Fe-doped thin films [43]. In addition, the value of k decreases with the increase of Fe doping owing to the improvement of surface smoothness which implies the increment of the transmitting capability (as, $A+T+R=1$). Hence absorbance decreases as Fe (4%, 6%, 8%) content increases in the TiO_2 thin film [44].

The complex dielectric constant (ϵ) expresses the relation between electromagnetic rays with matter [45]. ϵ equals to $(\epsilon_r + i\epsilon_i)$, where ϵ_r is the real part and ϵ_i is the imaginary part of dielectric constant expressed through the given relations,

$$\epsilon_r = n^2 - k^2 \quad (18)$$

$$\epsilon_i = 2nk \quad (19)$$

A plot of ϵ_r and ϵ_i with λ is shown in fig. 11. ϵ_r is related to the speed of light in the medium and ϵ_r is related to the transparency of medium. Both ϵ_r and ϵ_i have higher values in 2% Fe doped samples. This can be ascribed as the light absorption increases because of dipole motion or free carriers absorption [46]. From the diagram 11, it is clearly seen that $\epsilon_r \gg \epsilon_i$. The overall lower value of ϵ means that the material is more transmissive [43][47][48]. The nature of ϵ_i has a similar trend as of k which is related to the absorbance [49].

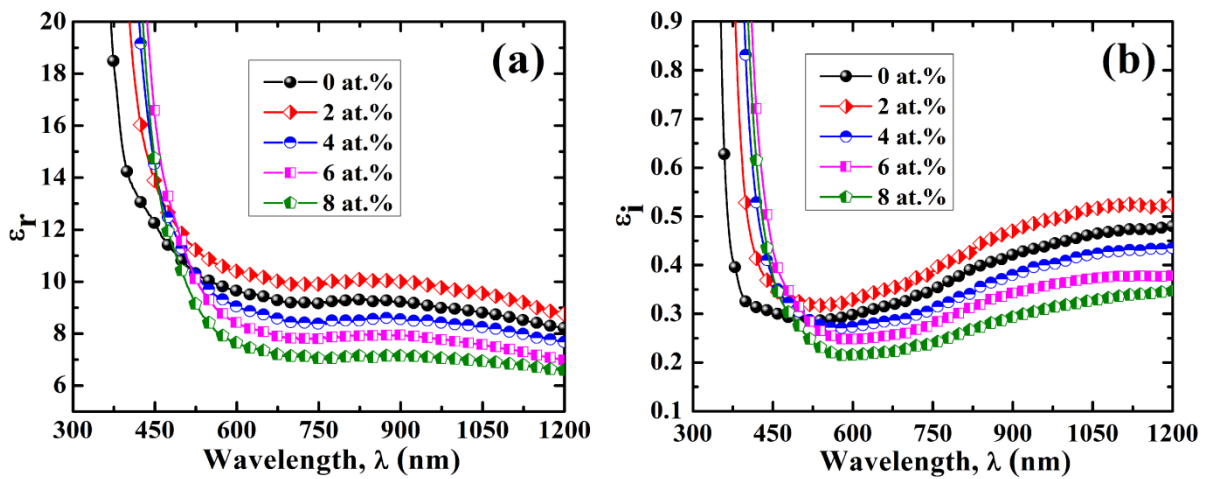


Figure 11. Plot of (a) ϵ_r and (b) ϵ_i of ϵ with wavelengths

The knowledge and data about the real and imaginary parts of the complex dielectric constant give the value of loss factor ($\tan\delta$) which is defined as.

$$\tan\delta = \frac{\epsilon_i}{\epsilon_r} \quad (20)$$

$\tan\delta$ is displayed with wavelength in Fig. 12 which reveals that the loss factor increases as λ increases, i.e., when light with high energy incident on the material the loss factor decrease [12][50]. At low frequency, the dielectric loss is very high because of the presence of electronic, ionic, dipolar, and space charge polarization [51]. The loss factor increases in the case of 2% Fe adulteration in TiO_2 due to the random distribution of Fe contents in TiO_2 crystal framework [46].

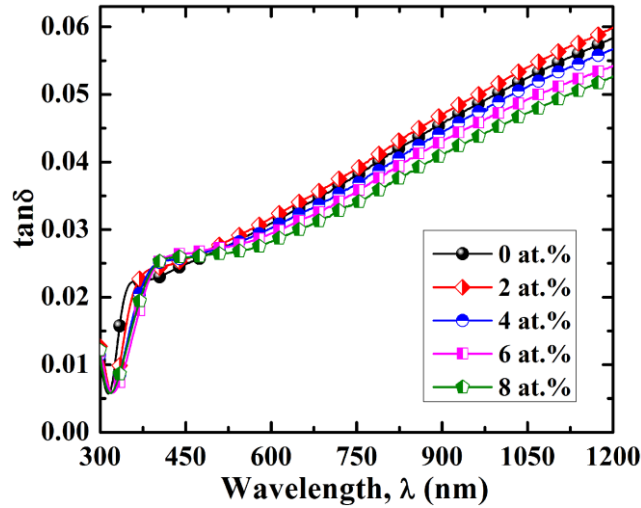


Figure 12. Deviation of $\tan\delta$ as a function of λ

The decrease of loss energy with the increase of Fe-content (4%-8%) in the samples which implies that carriers' concentration increases and they absorb more energy [42].

The real and imaginary dielectric constants are also used to determine the characteristics of the volume energy loss factor (VELF) and surface energy loss factor (SELF). The relations are given below,

$$\text{VELF} = \frac{\epsilon_i}{\epsilon_r^2 + \epsilon_i^2} \quad (21)$$

$$\text{SELF} = \frac{\epsilon_i}{(\epsilon_r + 1)^2 + \epsilon_i^2} \quad (22)$$

The plots of VELF and SELF are shown in the Fig. 13. VELF and SELF inform us about the probability of energy loss of fast-moving electrons through the bulk and surface of the material [52][53]. From Fig.13, it is observed that VELF and SELF have a similar pattern and their values decrease as photon energy increases. VELF is greater than SELF for both pristine and Fe-doped TiO_2 . This occurs because the motion of electrons within the samples relies on the amalgamate of cluster [54].

The relation among refractive index (n), lattice dielectric constant (ϵ_L) and wavelength (λ) can be written as, [47]

$$\epsilon = n^2 = \epsilon_L - \left(\frac{e^2 N}{4\pi c^2 \epsilon_0 m^*} \right) \lambda^2 \quad (23)$$

Where c = the velocity of light, ϵ_0 = DC in the free space ($\epsilon_0 = 8.854 \times 10^{-12}$ F/m), e = electric charge. In formula (23) N/m^* can be expressed as

$$\frac{N}{m^*} = \frac{\text{freecarrierdensity}}{\text{freecarriereffectivemass}} \quad (24)$$

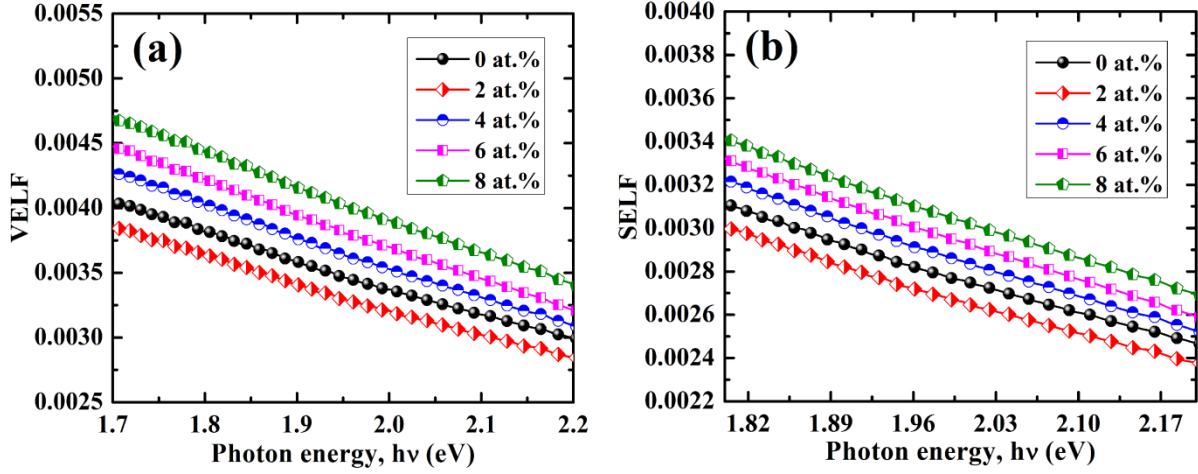


Figure 13. Variation of (a) VELF and (b) SELF with hv

Fig. 14 reveals the linear relationship of n^2 with λ^2 for different Fe contents. The y-intercept ($y=0$) gives the value of ϵ_L which is noticed to increase after 2 at.% Fe impurity and then decreases as the Fe content increases (Table 4).

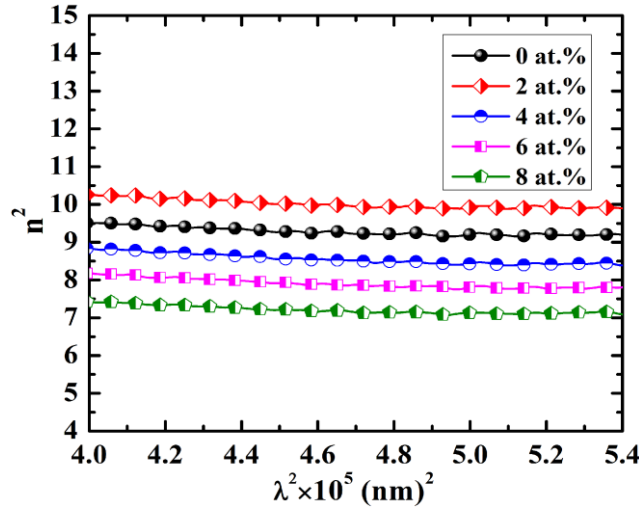


Figure 14. Relation between n^2 with λ^2

To get the idea of density and structure of the material it is essential to find the values of static refractive index (n_0) [47]. The high-frequency dielectric constant, ϵ_∞ can be evaluated from the static refractive index, n_0 which is known as the Sellmeier oscillator [52].

$$\frac{n_0^2 - 1}{n^2 - 1} = 1 - \left(\frac{\lambda_0}{\lambda}\right)^2 \quad (24)$$

Where λ_0 is the average oscillator wavelength. Figure 15 depicts the plot of $(n^2-1)^{-1}$ vs λ^{-2} which reveals a linear equation like $y=mx+c$, where λ^{-2} and $(n^2-1)^{-1}$ have been drawn in the horizontal and vertical directions, respectively. From the y-intercept, we can determine the static refractive index, n_0 . Moreover, by evaluating the slope of the line we can calculate the average oscillator wavelength λ_0 . The high frequency dielectric constant, ϵ_∞ can be estimated by using the following relation [12]

$$n_0 = \sqrt{\epsilon_\infty} \quad (25)$$

In addition, the average oscillator energy (S_0) has been evaluated from the following relation [45]

$$S_0 = \frac{n_\infty^2 - 1}{\lambda_0^2} \quad (26)$$

The estimated values of S_0 , λ_0 , n_0 , ϵ_L , and ϵ_∞ are tabulated in the Table 4 and their variations are depicted in the Fig. 16. It has been noticed from the Fig. 16 all the parameters follows the similar trends [12][47]. From the Table 4 it is observed that the value of S_0 is maximum for 2% Fe doped samples. It can be attributed that high value of S_0 means high crystalline behaviour among the Fe doped samples [47].

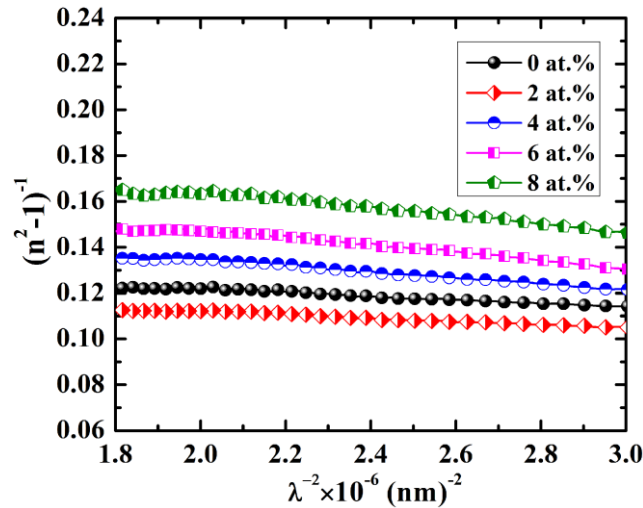


Figure 15. Relation between $(n^2-1)^{-1}$ and λ^{-2} of TiO_2 films

Table 4. Numerous optical dielectric parameters of pristine and Fe-doped titanium dioxide.

Fe contents (at.%)	ϵ_L	ϵ_∞	n_0	λ_0 (nm)	$S_0 \times 10^{13}$	$N/m^* \times 10^{20}$ ($\text{m}^{-3}\text{kg}^{-1}$)
0	10.38	8.21	2.87	244.71	12.09	1.46
2	11.21	8.85	2.97	244.32	13.10	1.60
4	10.01	7.19	2.68	288.70	7.42	1.94
6	9.21	6.47	2.54	307.90	5.75	1.73
8	8.24	5.95	2.44	302.32	5.42	1.37

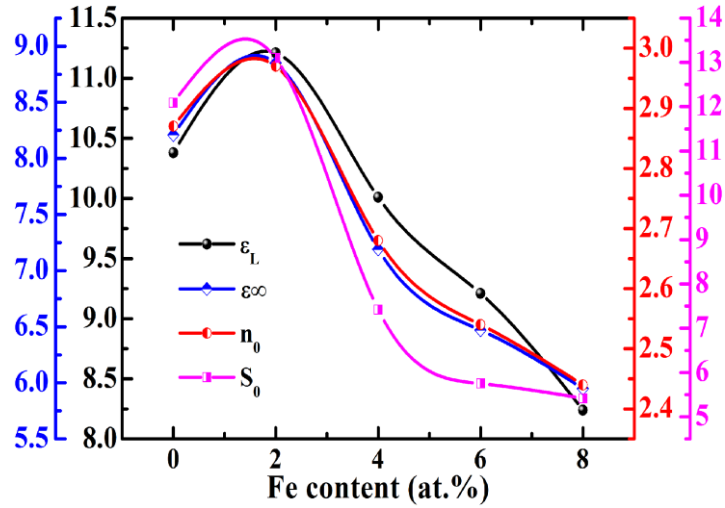


Figure 16. A comparison of ϵ_L , ϵ_∞ , n_0 and S_0 as a function of Fe contents.

3.3 Dispersion behavior of TiO₂ thin films:

It is very crucial to study the dispersion parameters of TiO₂ thin films as it gives important ideas to design the practical devices of optical communication and spectral dispersion. It is obvious to know the dispersive behaviour of TiO₂ to understand whether TiO₂ thin films are potential candidate for practical uses. We have employed the Wemple and DiDomenico (W–D) model. According to this model refractive index is plotted according to the following relation [44][55]:

$$n^2 - 1 = \frac{E_0 E_d}{E_0^2 - (hv)^2} \quad (27)$$

Where E_0 is the single oscillator energy and E_d is the dispersion energy parameter which measures the average bandgap energy ($E_0 = 1.5E_g$) and the average strength of the interband optical transitions respectively. The energy dispersion parameter E_d is connected with the harmonization of positive ions closed to each other, ionicity, anion valency, and the efficient quantity of diffusion electrons [47][56]. Considering the above equation (27), a diagram of $(n^2 - 1)^{-1}$ vs $(hv)^2$ has been depicted in Fig. 17. By estimating the y-intercept and slope from the $(n^2 - 1)^{-1}$ vs $(hv)^2$ plot the value of E_d and E_0 are calculated, respectively.

The highest value of E_d has been noticed for 2 at.% Fe doped sample which is related to the structural changes of the thin film [47]. The value of E_d decreases (for 4, 6 and 8 at.% of Fe content) which implies that the co-ordination number of atoms decreases. The value of E_0 decreases with the increase of Fe element as a dopant in TiO₂ which may be due to the increase of scattering centre and the decrease of E_g [12].

In order to get a better understanding and knowledge of the ionic bond strength of a material it is very important to investigate another energy parameter known as lattice energy (E_L). Lattice energy E_L related to the above discussed energy parameters E_0 and E_d can be estimated from the equation [57].

$$n^2 - 1 = \frac{E_0 E_d}{E_0^2 - E^2} - \frac{E_1^2}{E^2} \quad (28)$$

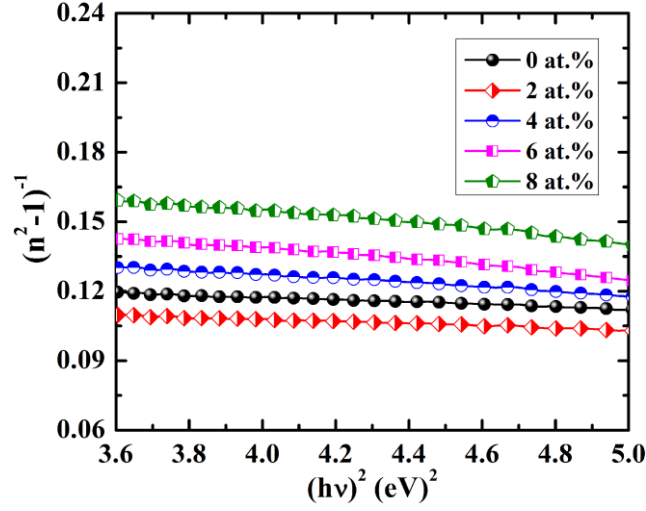


Figure 17. Plot of $(n^2-1)^{-1}$ vs $(hv)^2$ for pristine and Fe-doped TiO_2

In the lower energy region where the wavelength is longer than phonon resonance, means $E_0^2 \gg E^2$. $(n^2 - 1)$ is plotted against $(hv)^{-2}$ (Fig. 18) which will be a straight line according to Poignant [45][58] in the long-wavelength region. Considering this approximation one can write the above expression in the following form,

$$n^2 - 1 = \frac{E_d}{E_0} - \frac{E_1^2}{E^2} \quad (29)$$

The y-intercept gives $\frac{E_d}{E_0}$ and the slope of the line is equal to $-E_1^2$. From the calculation of slope, the lattice energy parameter can easily be determined.

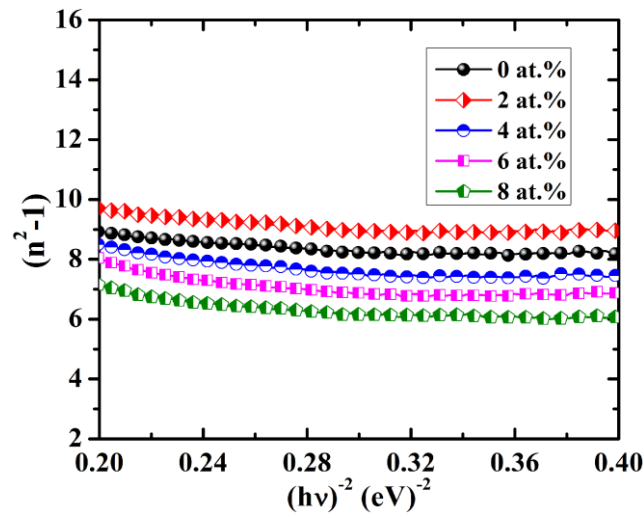


Figure 18. Variation of (n^2-1) with $(hv)^{-2}$

Table 5. Dispersion energy parameters of pristine and Fe-doped titanium dioxide samples

Fe contents (at.%)	E_g (eV)	E_d (eV)	E_0 (eV)	E_1 (eV)	E_0/E_g
0	3.81	38.25	5.25	2.31	1.38
2	3.76	41.86	5.27	2.40	1.40
4	3.72	26.51	4.30	2.74	1.16
6	3.71	20.71	3.90	2.83	1.05
8	3.70	19.26	3.98	2.59	1.08

3.4 Conclusion

In summary, a general overview of synthesis and characterizations of pure and Fe doped TiO₂ thin films has been presented in this paper and cost effective spray pyrolysis route has been employed to synthesize the samples meticulously. XRD study shows the pure and Fe doped samples are nano structured. A phase transition, anatase phase to mixed phase has been confirmed from the XRD, when TiO₂ is adulterated by Fe (4%, 6% and 8%). A through investigation of microstructural parameters like crystallite size, strain, dislocation density are performed by D-S, W-H, and H-W methods. The investigated results reveals that when the doping concentration is increased from 0 to 8 at. % the crystallite size declined from $D_S = 31.82$ to 17.26 nm, $D_{WH} = 34.14$ to 18.46 nm and $D_{HW} = 30.54$ to 16.18 nm, while the strain was found to decrease from $\epsilon_{WH} = 1.36$ to $2.07, \times 10^{-3}$ and $\epsilon_{HW} = 1.09$ to $2.40, \times 10^{-3}$, respectively. From the UV vis spectra, it is observed that the absorption edge of Fe-doped TiO₂ products is shifted towards longer wavelengths (i.e. red shifted) which causes the reduction of bandgap from 3.81 eV to 3.70 eV. Other optical parameters like dielectric constants, refractive index, energy loss factor, SELF, VELF and lattice energy are estimated. The Fe-doped TiO₂ thin films may be considered as a promising and effective candidate in designing and manufacturing electronic devices.

Acknowledgments

We acknowledged the Department of Physics, Department of Glass and Ceramic Engineering, Bangladesh University of Engineering and Technology (BUET), Dhaka, Bangladesh, and also Bangladesh Atomic Energy Center, Dhaka, Bangladesh Atomic Energy Commission (BAEC) for their cordial supports.

Declaration of interests

We certify that this manuscript has not yet been submitted to any journal and there are no affiliations with or involvement in any organization or entity with any financial interest in the subject matter or materials discussed in this manuscript.

References

- [1] Kumar M, Kumar D and Gupta A K 2015 Fe-Doped TiO₂ Thin Films for CO Gas Sensing *Journal of Electronic Materials* **44** 152–7
- [2] Ramadoss A and Kim S J 2013 Vertically aligned TiO₂ nanorod arrays for electrochemical supercapacitor *Journal of Alloys and Compounds* **561** 262–7
- [3] Jeong S H, Kim J K, Kim B S, Shim S H and Lee B T 2004 Characterization of SiO₂ and TiO₂ films prepared using rf magnetron sputtering and their application to anti-reflection coating *Vacuum* **76** 507–15
- [4] Alasaarela T, Saastamoinen T, Hiltunen J, Säynätjoki A, Tervonen A, Stenberg P, Kuittinen M and Honkanen S 2010 Atomic layer deposited titanium dioxide and its application in resonant waveguide grating *Applied Optics* **49** 4321–5
- [5] Touam T, Atoui M, Hadjoub I, Chelouche A, Boudine B, Fischer A, Boudrioua A and Doghmane A 2014 Effects of dip-coating speed and annealing temperature on structural, morphological and optical properties of sol-gel nano-structured TiO₂ thin films *EPJ Applied Physics* **67** 30302–6
- [6] Chen K M, Sparks A W, Luan H C, Lim D R, Wada K and Kimerling L C 1999 SiO₂/TiO₂ omnidirectional reflector and microcavity resonator via the sol-gel method *Applied Physics Letters* **75** 3805–7
- [7] WON D-J, WANG C-H and Doo-Jin CHOI 2001 Characteristics of Metal/Ferroelectric/Insulator/Semiconductor Using La₂O₃ Thin Film as an Insulator *Japanese Journal of Applied Physics* **40** 1235–7
- [8] Paul T C and Podder J 2019 Synthesis and characterization of Zn-incorporated TiO₂ thin films: impact of crystallite size on X-ray line broadening and bandgap tuning *Applied Physics A: Materials Science and Processing* **125** 818
- [9] Arunachalam A, Dhanapandian S and Manoharan C 2016 Effect of Sn doping on the structural, optical and electrical properties of TiO₂ films prepared by spray pyrolysis *Journal of Materials Science: Materials in Electronics* **27** 659–676
- [10] Houg B, Liu C C and Hung M T 2013 Structural, electrical and optical properties of molybdenum-doped TiO₂ thin films *Ceramics International* **39** 3669–76
- [11] Magdalane C M, Kanimozhi K, Arularasu M V, Ramalingam G and Kaviyarasu K 2019 Self-cleaning mechanism of synthesized SnO₂/TiO₂ nanostructure for photocatalytic activity application for waste water treatment *Surfaces and Interfaces* **17** 100346
- [12] Paul T C, Podder J and Babu M H 2020 Optical constants and dispersion energy parameters of Zn-doped TiO₂ thin films prepared by spray pyrolysis technique *Surfaces and Interfaces* **21** 100725
- [13] Kim D H, Hong H S, Kim S J, Song J S and Lee K S 2004 Photocatalytic behaviors and structural characterization of nanocrystalline Fe-doped TiO₂ synthesized by mechanical alloying *Journal of Alloys and Compounds* **375** 259–64
- [14] Patil L A, Suryawanshi D N, Pathan I G and Patil D M 2013 Nickel doped spray pyrolyzed nanostructured TiO₂ thin films for LPG gas sensing *Sensors and Actuators, B: Chemical* **176** 514–21
- [15] Paul T C, Babu M H, Podder J, Dev B C, Sen S K and Islam S 2021 Influence of Fe³⁺ ions doping on TiO₂ thin films: Defect generation, d-d transition and band gap tuning for optoelectronic device applications *Physica B: Physics of Condensed Matter* **604** 412618
- [16] Huang F, Li Q, Thorogood G J, Cheng Y-B and Caruso R A 2012 Zn-doped TiO₂ electrodes in dye-sensitized solar cells for enhanced photocurrent *J. Mater. Chem.* **22** 17128–32

- [17] Sood S, Umar A, Mehta S K and Kansal S K 2015 Highly effective Fe-doped TiO₂ nanoparticles photocatalysts for visible-light driven photocatalytic degradation of toxic organic compounds *Journal of Colloid and Interface Science* **450** 213–23
- [18] Naveen C S, Raghu P, Mahesh H M, Rao K N, Kumar R R and Phani A R 2014 Optical and structural properties of highly porous shell structured Fe doped TiO₂ thin films *Rare metals* **33** 578–82
- [19] Ngaffo F F, Caricato A P, Fernandez M, Martino M and Romano F 2007 Structural properties of single and multilayer ITO and TiO₂ films deposited by reactive pulsed laser ablation deposition technique *Applied Surface Science* **253** 6508–11
- [20] Lin C Y W, Channei D, Koshy P, Nakaruk A and Sorrell C C 2012 Effect of Fe doping on TiO₂ films prepared by spin coating *Ceramics International* **38** 3943–6
- [21] Nejand B A, Sanjabi S and Ahmadi V 2010 Optical and Photocatalytic Characteristics of Nitrogen Doped TiO₂ Thin Film Deposited by Magnetron Sputtering *Transaction F: Nanotechnology* **17** 102–7
- [22] Kobayashi S and Ichimura M 2018 Electrochemical deposition of Cu-doped p-type iron oxide thin films *Semiconductor Science and Technology* **33** 105006
- [23] Shalan A E and Rashad M M 2013 Incorporation of Mn²⁺ and Co²⁺ to TiO₂ nanoparticles and the performance of dye-sensitized solar cells *Applied Surface Science* **283** 975–81
- [24] Chauhan R, Kumar A and Chaudhary R P 2012 Structural and optical characterization of Zn doped TiO₂ nanoparticles prepared by sol-gel method *Journal of Sol-Gel Science and Technology* **61** 585–91
- [25] Manurung P, Putri Y, Simanjuntak W and Low I M 2013 Synthesis and characterisation of chemical bath deposited TiO₂ thin-films *Ceramics International* **39** 255–9
- [26] Naffouti W, Jrad A, Ben Nasr T, Ammar S and Turki-Kamoun N 2016 Structural, morphological and optical properties of TiO₂:Mn thin films prepared by spray pyrolysis technique *Journal of Materials Science: Materials in Electronics* **27** 4622–30
- [27] Das S C, Green R J, Podder J, Regier T Z, Chang G S and Moewes A 2013 Band gap tuning in ZnO through Ni doping via spray pyrolysis *Journal of Physical Chemistry C* **117** 12745–53
- [28] Weng W, Ma M, Du P, Zhao G, Shen G, Wang J and Han G 2005 Superhydrophilic Fe doped titanium dioxide thin films prepared by a spray pyrolysis deposition *Surface & Coatings Technology* **198** 340–4
- [29] Jereil S D and Vijayalakshmi K 2015 Effect of Fe doping on the properties of TiO₂ thin films for ethanol sensing application *Nano Vision* **5** 69–76
- [30] Kumar P M R, Kartha C S, Vijayakumar K P, Abe T, Kashiwaba Y, Singh F and Avasthi D K 2005 On the properties of indium doped ZnO *Semiconductor Science and Technology* **20** 120
- [31] Sen S K, Paul T C, Dutta S, Matin M A, Islam M F and Hakim M A 2019 Effect of gamma (γ -) irradiation on the structural, morphological, optical and electrical properties of spray pyrolysis-deposited h-MoO₃ thin films *Surfaces and Interfaces* **17** 100377
- [32] Sen S K, Paul T C, Manir M S, Dutta S, Hossain M N and Podder J 2019 Effect of Fe-doping and post annealing temperature on the structural and optical properties of -MoO₃ nanosheets *Journal of Materials Science: Materials in Electronics* **30** 14355–14367
- [33] Dhanapandian S, Arunachalam A and Manoharan C 2016 Highly oriented and physical properties of sprayed anatase Sn-doped TiO₂ thin films with an enhanced antibacterial activity *Applied Nanoscience* **6** 387–97

- [34] Arunachalam A, Dhanapandian S, Manoharan C and Sridhar R 2015 Characterization of sprayed TiO₂ on ITO substrates for solar cell applications *Spectrochimica Acta - Part A: Molecular and Biomolecular Spectroscopy* **149** 904–12
- [35] Prakash N G, Dhananjaya M, Narayana A L, Maseed H, Srikanth V V S S and Hussain O M 2019 Improved electrochemical performance of rGO-wrapped MoO₃ nanocomposite for supercapacitors *Applied Physics A* **125** 488–97
- [36] Manzoor S, Husain S, Somvanshi A, Fatema M and Zarrin N 2019 Exploring the role of Zn doping on the structure , morphology , and optical properties of- LaFeO₃ *Applied Physics A* **125** 509–19
- [37] Moradi H, Eshaghi A, Hosseini S R and Ghani K 2016 Fabrication of Fe-doped TiO₂ nanoparticles and investigation of photocatalytic decolorization of reactive red 198 under visible light irradiation *Ultrasonics Sonochemistry* **32** 314–9
- [38] Rozati M Y S M and Najafi N 2020 Investigation of the effect of temperature on the structural , optical , electrical , and self - cleaning properties of ITO thin films *Applied Physics A* **126** 523
- [39] Vijayalakshmi K and David Jereil S 2015 Enhanced ethanol sensing performance of Fe: TiO₂ nanowires and their mechanism of sensing at room temperature *Ceramics International* **41** 3220–6
- [40] Sharmin M and Podder J 2019 Influence of Al doping on the structure and properties of Fe₂O₃ thin films: high transparency, wide band gap, ferromagnetic behavior *Semiconductor Science and Technology* **34** 075033
- [41] Sharmin M and Bhuiyan A H 2018 Influence of substrate temperature on the properties of spray deposited nanofibrous zinc oxide thin films *Applied Physics A* **124** 57–67
- [42] Majeed Khan M A, Wasi Khan M, Alhoshan M, Alsalhi M S and Aldwayyan A S 2010 Influences of Co doping on the structural and optical properties of ZnO nanostructured *Applied Physics A: Materials Science and Processing* **100** 45–51
- [43] Chalana S R, Ganesan V and Pillai V P M 2015 Surface plasmon resonance in nanostructured Ag incorporated ZnS films *AIP ADVANCES* **5** 107207
- [44] Datta J, Layek A, Das M, Dey A, Middya S, Jana R and Ray P P 2017 Growth of hierarchical strontium incorporated cadmium sulphide for possible application in optical and electronic devices *Journal of Materials Science: Materials in Electronics* **28** 2049–61
- [45] Abdel-Baki M, Wahab F A A and El-Diasty F 2006 Optical characterization of xTiO₂-(60 - X)SiO₂-40Na₂O glasses: I. Linear and nonlinear dispersion properties *Materials Chemistry and Physics* **96** 201–10
- [46] Kamruzzaman M, Uddin K and Podder J 2014 Synthesis and characterization of Zn_{1-x}Cd_xS thin films prepared by the spray pyrolysis technique *Asian Journal of Applied Sciences* **7** 607–20
- [47] Usha K S, Sivakumar R and Sanjeeviraja C 2013 Optical constants and dispersion energy parameters of NiO thin films prepared by radio frequency magnetron sputtering technique *Journal of Applied Physics* **114** 123501
- [48] Vs G K and Mg M 2020 Characterization of spray deposited ternary Zn_xS_{1-x}Se thin films for solar cell buffers *Surfaces and Interfaces* **20** 100509
- [49] Al-Saadi T M, Hussein B H, Hasan A B and Shehab A A 2019 Study the Structural and Symposium Optical Properties of Cr Nanoparticles Synthesized by Sol-Gel Method *Energy Procedia* **157** 457–65
- [50] Sagadevan S and Podder J 2015 Optical and Electrical Properties of Nanocrystalline SnO₂ Thin Films Synthesized by Chemical Bath Deposition Method *Soft Nanoscience Letters* **5** 55–64

- [51] Archana R, Sudhahar S, Sadayandi K, Vidhya M, Sagadevan S, Mohammad F and Podder J 2020 Investigation of the optical, photoluminescence, and dielectric properties of P-Toluidinium picrate single crystals *Chinese Journal of Physics* **67** 283–92
- [52] Arasu P A and Williams R V 2015 Effect of annealing temperature on structural and optical parameters of sol-gel routed molybdenum oxide thin film *Surface Review and Letters* **22** 1–8
- [53] Akl A A and Mahmoud S A 2018 Effect of growth temperatures on the surface morphology, optical analysis, dielectric constants, electric susceptibility, Urbach and bandgap energy of sprayed NiO thin film *Optik - International Journal for Light and Electron Optics* **172** 783–93
- [54] Akl A A, Mahmoud S A and Salman S M M 2018 Surface Morphology , Optical Conductivity , Localized States and Dielectric Constants of Sprayed Nickel Oxide Films at Different Substrate Temperatures *International Journal of Science and Research (IJSR)* **7** 935–43
- [55] MaÂrqueza E, Bernal-Olivaa A M, GonzaÂlez-Leala J M, Prieto-AlcoÂna R, Ledesmaa A, JimeÂnez-Garaya R and MaÂrtel I 1999 Optical-constant calculation of non-uniform thickness thin films of the Ge₁₀As₁₅Se₇₅ chalcogenide glassy alloy in the sub-band-gap region (0.1-1.8 eV) *Materials Chemistry and Physics* **60** 231–9
- [56] Wemple S H and DiDomenico M 1971 Behavior of the electronic dielectric constant in covalent and ionic materials *Physical Review B* **3** 1338–51
- [57] Wemple S H 1979 Material dispersion in optical fibers *Applied Optics* **18** 31
- [58] H. Poignant 1981 Dispersive and scattering properties of a ZrF₄ based glass *Electronics Letters* **17** 1–2